Estuarine, Coastal and Shelf Science 324 (2025) 109445

Contents lists available at ScienceDirect

Estuarine, Coastal and Shelf Science

journal homepage: www.elsevier.com/locate/ecss

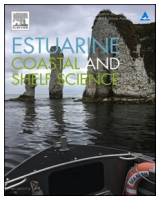

Submarine groundwater discharge into a temperate tidal basin: Mapping and characterization by a multi-method and multi-scale approach

Ercan Erkul [a,*], Tina Wunderlich [a], Dennis Wilken [a], Jan Igel [b], Mike Müller-Petke [b], Mathias Ronczka [b], Tobias Splith [b], Simon Fischer [a], Benjamin Gilfedder [c], Michael Ernst Böttcher [d,e,f], Cátia M. Ehlert von Ahn [d,g], Ralf Gründling [h], Jasper Hoffmann [i,j], Anna-Kathrina Jenner [d], Erman Lu [a], Till Oehler [g], Wolfgang Rabbel [a], Lasse Sander [i], Jan Scholten [a], Franz Schulze [h], Nils Moosdorf [a,g], Ulf Mallast [h]

[a] Institute of Geosciences - IfG, University of Kiel, Kiel, Germany
[b] Leibniz Institute for Applied Geophysics - LIAG, Hannover, Germany
[c] Department of Hydrology, Faculty of Regional and Environmental Sciences, University of Trier, Trier, Germany
[d] Geochemistry & Isotope Biogeochemistry Group, Leibniz Institute for Baltic Sea Research (IOW), Warnemünde, Germany
[e] Institute for Geography & Geology, University of Greifswald, Greifswald, Germany
[f] Interdisciplinary Faculty, University of Rostock, Rostock, Germany
[g] Leibniz-Centre for Tropical Marine Research (ZMT), Bremen, Germany
[h] Helmholtz-Centre for Environmental Research - UFZ, Leipzig, Germany
[i] Alfred Wegener Institute, Helmholtz Centre for Polar and Marine Research - AWI, Sylt, Germany
[j] Marine Geology and Seafloor Surveying Group, Department of Geosciences, University of Malta, Msida, Malta

A R T I C L E I N F O

Keywords:
Submarine Groundwater Discharge (SGD)
aerial orthophoto
Electromagnetic Induction (EMI)
Electrical Resistivity Tomography (ERT)
Nuclear Magnetic Resonance (NMR)
Pore water salinity

A B S T R A C T

Submarine groundwater discharge (SGD) is considered as an important source of chemical substances to the oceans. Investigations of SGD need to consider varying spatial and temporal scales. They remain a challenge and require the application of different complementary detection and quantification methods. Our study focuses on the identification of fresh SGD (FSGD) in intertidal zones using the Königshafen Bay on the island Sylt, Germany, as an example case. We applied geophysical, remote sensing and in-situ pore water measurements to develop a suitable combination of survey methods for an efficient detection of FSGD. Our results provide detailed information on the occurrence and spreading of FSGD at scales ranging from meters to kilometers. We propose a stepwise approach to identify FSGD in intertidal zones as follows: First, orthophotos from unmanned aerial vehicles (UAVs) can highlight distinct tidal flat features characterized by brighter surrounding sediments and typical plant growth at possible FSGD sites. These can be mapped by large-scale electromagnetic induction (EMI), where possible FSGD patches appear as areas of higher electrical resistivity. Ground penetrating radar (GPR) can then be used to check the possible FSGD patches directly on the surface with high lateral resolution. The deep structure of FSGD can then be explored with Electrical Resistivity Tomography (ERT) on targeted profiles to detect fresh water in the sediment through the zone of increased electric resistivity. Additional Nuclear Magnetic Resonance (NMR) measurements from the surface will help to estimate the water content of the sediments and to distinguish between clay layers and salt water containing sand layers. Finally, the geophysical results are verified by in-situ measurements of pore water salinity. Using this approach, 17 significant areas with FSGD sites in the Königshafen bay could be efficiently identified. These areas have a diameter of 30–60 m and are characterized by increased electrical resistivities of 5 Ωm to 30 Ωm and decreased salinity of 0–10 PSU with respect to the surrounding saltwater-saturated areas.

This article is part of a special issue entitled: Sustaining sandy beach systems published in Estuarine, Coastal and Shelf Science.

* Corresponding author.
E-mail address: ercan.erkul@ifg.uni-kiel.de (E. Erkul).

https://doi.org/10.1016/j.ecss.2025.109445
Received 16 January 2025; Received in revised form 16 July 2025; Accepted 18 July 2025
Available online 23 July 2025

1. Introduction

Submarine groundwater discharge (SGD) is a pathway for water and chemicals from land to the ocean. Studies at different locations worldwide have demonstrated the significance of SGD as a potential source of nutrients and dissolved carbon species to coastal ecosystems (e.g. Johannes and Hearn, 1985; D'Elia et al., 1981; Moore, 2010; Waska and Kim, 2011; Oehler et al., 2021; Moosdorf et al., 2015, 2021; Böttcher et al., 2024; Szymczycha et al., 2023; Wilson et al., 2024). Likewise, SGD plays a potentially critical role in coastal ecology (Lecher and Mackey, 2018), inter alia through changing local light attenuation by coupling nutrients and phytoplankton (Cyronak et al., 2013), or intensifying ocean acidification (Garrison et al., 2003). Although the significance of SGD is well established, existing flux data is highly uncertain. These uncertainties arise from upscaling local point measurements to regional scales (e.g., Mejías et al., 2012; Povinec et al., 2012) or from model-based estimations of regional or global fluxes (e.g., Moore et al., 2008; Kwon et al., 2014).

SGD consists of a terrestrial derived freshwater component (FSGD), and a recirculated seawater component from the seabed. (Taniguchi, 2002; Burnett et al., 2006; Santos et al., 2012; Kreuzburg et al., 2023). These two components mix in the subterranean estuary (Moore, 1999). Meteoric groundwater that discharges below sea level is considered fresh SGD (FSGD) (Luijendijk et al., 2020). FSGD is driven by the hydraulic gradient between land and sea, while recirculating seawater is driven by pressure-induced mechanisms such as waves, tides, storm surges and density-driven flow.

Conventional methods for determining SGD, e.g. pore water sampling in the subsurface, usually require wells or piezometers to be drilled or hammered into the subsurface. Sampling pore water in-situ in this way is labor intensive and limited to suitable hydrodynamic conditions. Although the spatial resolution is limited, especially in the horizontal plane. On the other hand, this method is able to provide high-resolution results on the characteristics of SGD on the local scale.

Geophysical methods provide a rapid, non-invasive approach to spatial mapping of subsurface salinity through measuring the bulk electrical resistivity of the subsurface water saturated sediments. The bulk electric resistivity depends critically on the electric resistivity of the pore water, which is much greater for fresh water (typically 10 to 30 Ωm) than for seawater (typically 0.2 to 1 Ωm). Especially geoelectric depth sounding is an attractive approach for complementing standard subsurface penetration techniques (in-situ pore water sampling) because it provides tomographic depth profiles of electric resistivity. Suitable methods of geoelectric sounding are DC-electric resistivity tomography (ERT) and electromagnetic induction (EMI) measurements. ERT and EMI soundings can be performed almost continuously with meter-to deca-meter spacing and sounding depths down to several tens (ERT) up to hundreds (EMI) meter depth penetration. Therefore, ERT and EMI profiling is a valuable tool complementing pointwise measurements of pore water sampling and enabling meter-to kilometer-scale investigations of FSGD and related hydrological model building for understanding the spatial discharge distribution, in which ecological, hydrological and chemical processes take place. Both methods can be applied onshore, meaning land-based during low tide, and offshore (Müller, 2010; Müller et al., 2011; Hermans and Paepen, 2020; Hoffmann et al., 2025). Airborne EMI surveying has been used extensively for mapping aquifer structures, and for delineating bottom and groundwater salinity from saltwater intrusion into coastal aquifers (e.g., Siemon, 2006; Steuer et al., 2007). Moreover, EMI can also be applied from the ground surface by walking using frequency-domain instruments measuring the apparent electrical resistivity for local studies that need higher spatial resolution which helicopter-based applications cannot provide (Hoffmann et al., 2025).

Ground-penetrating radar (GPR) is based on the emission and reflection of electromagnetic waves and used for high-resolution subsurface investigation (Annan, 2009). On-land GPR can provide spatial information on the groundwater table and shallow aquifer architecture and characteristics in coastal environments (Igel et al., 2013), and specifically in the context of SGD (Luoma et al., 2021). Due to the high attenuation of electromagnetic waves in saline environments, GPR has not been used in the intertidal so far, however, analyzing the signal amplitudes can give an indirect differentiation between fresh and saline pore water in such environments.

Nuclear-Magnetic-Resonance (NMR) serves for characterizing the sediment structure in terms of porosity and hydraulic conductivity and is commonly used to investigate shallow sedimentary groundwater systems up to 150 m depth. It can be applied from the surface and downhole (e.g. Behroozmand et al., 2015; Müller-Petke and Yaramanci, 2015). In coastal environments the joint application of NMR with ERT or EMI allows to distinguish salt-water saturated aquifers from clayey aquitards, which would be difficult by electrical resistivity alone. However, NMR is mostly used for downhole depth profiling as mapping approaches (2D, 3D) are time consuming (Jiang et al., 2015).

In addition to geophysical methods applied on larger areas, unmanned aerial vehicles (UAVs) have proven to be valuable tools in mapping SGD, particularly when employing thermal sensors (Tamborski et al., 2015; Lee et al., 2016; Mallast and Siebert, 2019; Oberle et al., 2022; Röper et al., 2014). These sensors detect differences in skin sea surface temperature caused by the inflow of groundwater, which often exhibits a distinct temperature contrast compared to the surrounding water (Mallast et al., 2014). The effectiveness of this approach is also influenced by the volume of discharge, as higher volumes tend to have a greater impact. However, in tidal areas characterized by their dynamic nature and the absence of a continuous water column, the use of thermal sensors for SGD detection is challenging, as the influence of groundwater temperature on the ambient sediment is reduced. However, since SGD may significantly alter seafloor morphology (Hoffmann et al., 2020, 2023), the high spatial resolution offered by UAVs presents opportunities to identify surface expressions that could serve as proxies for groundwater discharge over large areas. These surface expressions could include variations in sediment classification (Kim et al., 2019), vegetation types (such as seagrass) (Chand and Bollard, 2021), faunal imprints on sediment surface (Zipperle and Reise, 2005), or microtopography (Curcio et al., 2023). When combined with in-situ information on SGD, these proxies can potentially be used to extrapolate potential SGD areas. Overall, the application of drones in SGD research holds promise for providing detailed spatial information and contributing to a better understanding of these complex coastal processes.

Therefore, the aim of this study is to develop and test a concept for exploring and investigating FSGD on scales from meters to kilometers using drones, ground-based geophysical sounding and pore water sampling. Our test location is the tidal back-barrier area of Königshafen Bay on the island of Sylt, Germany, where we show how a combination of these methods can provide detailed information on the occurrence and distribution of SGD. The basic objectives of our multi-method approach are to map or determine the following complementary properties and characteristics of FSGD at the surface and in the shallow subsurface of the investigation area.

- to identify sediment color anomalies and seagrass areas from high-resolution images of the tidal flat through drone flights,
- to identify spatial variations of electrical resistivity in the subsurface layers at decimeter- and meter-scale resolution through EMI and ERT mapping.
- to determine depth functions of salinity from downhole pore-water sampling. Together with geoelectric measurements the salinity analysis serves for establishing an empirical site-specific relation between pore-water salinity and in-situ bulk electrical resistivity. This enables to identify possible FSGD spots on the electric resistivity map and to up-scale the point sampling from the drill holes to larger areas.

- to determine depth functions of the water content of the sediment layers from surface nuclear magnetic resonance (NMR) measurements for cross-checking and validating the geoelectric results.

1.1. Site description

Königshafen Bay is a tidal back-barrier environment located in the northern part of the island of Sylt, Germany, and forms part of the Wadden Sea National Park (Fig. 1a). To the north, west and south, the area is delimited by marine deposits covered by dunes (Lindhorst et al., 2008 und Lindhorst et al., 2010), while the island of Uthörn forms the eastern boundary. The bay has a size of approx. 4 km^2. Today, Königshafen is a shallow bay with water depths of mostly less than 1.5 m. In the central part of the bay, one tidal creek with depths of up to 5 m connects the shallow mudflats with the Lister Ley, one of the main tidal channels of the Sylt-Rømø Bight. The island of Sylt primarily formed over late Holocene time scales, in a setting entirely composed of permeable and unconsolidated sediment. Especially the landscapes in the northern part of the island can be regarded as relatively young (probably less than 2000 years old) and formed in a mix of variable (calm and energetic) sedimentary conditions (Lindhorst et al., 2013; Gripp and Simon, 1940). A comprehensive description of the facies below the modern tidal flats of Königshafen Bay is found in a baseline study by Bayerl and Higelke (1994). The modern surface deposits of the bight are composed of fine sediments in the inner part and coarse sediments towards the outer parts of the intertidal Königshafen Bay (Dolch and Hass, 2008). For example, dune sands and sand bar deposits are observed in coastal areas and fine sandy or muddy tidal sediments and clay horizons in the inner part (Austen, 1992; Goldschmidt et al., 1993) (Fig. 1).

Königshafen Bay is a natural system with well-defined hydrological boundaries and is ideal for SGD investigations, because it is an intertidal bay with only one outlet and no surface inflow (Reise et al., 2007). Previous knowledge exists from various fields such as morphological development, sedimentology (Fig. 1; Austen, 1990; Bayerl and Higelke, 1994; Dolch and Hass, 2008), benthic biogeochemistry (Böttcher and Al-Raei, unpublished data), distribution of biota (Reise et al., 2007). SGD occurrence was first mentioned in 1758 (Schmidt, 1974) and their relation to the biota was described by Zipperle and Reise (2005).

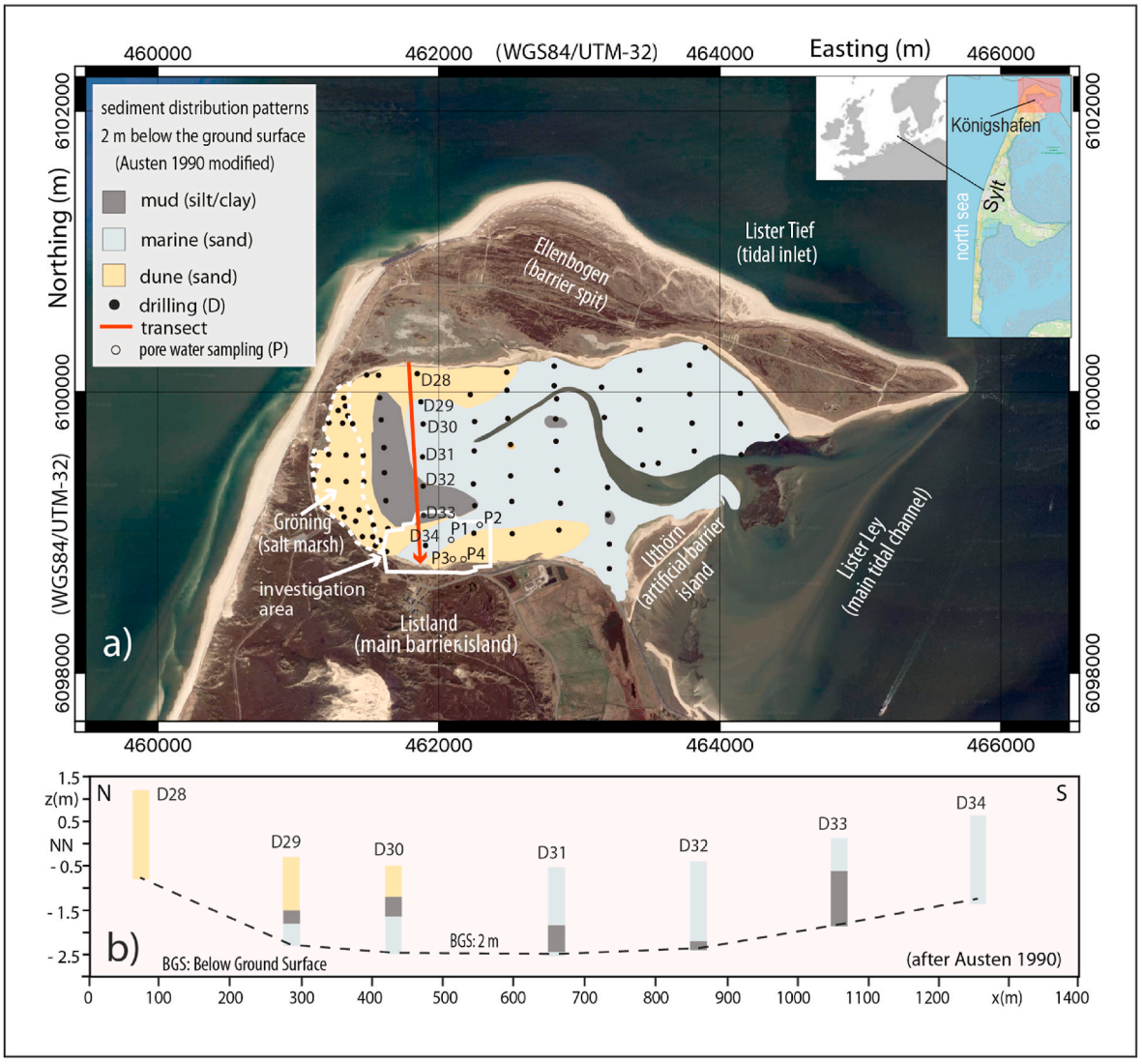

Fig. 1. (a) Location of the field site "Königshafen Bay" on the island of Sylt, in Northern Germany with inserted map of the sediment distribution patterns at a depth of 2 m from geological surface mapping and drillings in Königshafen bay (modified after Austen, 1990). The red line marks the location of the NS-transect and the white frame the investigation area. (b) Exemplary cross-section of sediment cores to illustrate the near-surface mudflat sediments in a north-south profile of Königshafen Bay (modified after Austen, 1990). (Basemap: ©Google Satellite, Data SIO, NOAA, U.S. Navy, NGA, GEBCO, Image, 2024 TerraMetrics). (For interpretation of the references to color in this figure legend, the reader is referred to the Web version of this article.)

The exemplary cross-section in Fig. 1b illustrates the near-surface mudflat sediments. It crosses the Königshafen Bay in north-south direction and has a length of approx. 1300 m. At this site, intertidal sandy sediments extend continuously down to approx. −3 m below NN. An extensive clay layer covers the tidal flat sand in this area and reaches a thickness of 2 m at 400 m from the southern shore. In the middle of the profile up to the surface, the clay layer is followed by intertidal sands, and by dune sands and sand-bar deposits in the northern nearshore regions (Bayerl and Higelke, 1994). According to Austen (1992), muddy (clay) intertidal sediment extends to the surface in the western part of Königshafen Bay ("Gröningwatt") (Fig. 1a) with a thickness of less than 1 m. At the north-western edge of Königshafen Bay, clay-silt deposits reach a thickness of more than 4 m.

2. Methods

The present study focuses on the southern part of Königshafen Bay (Fig. 2) and several methods were applied aerial orthophotos via UAVs, Electromagnetic Induction (EMI), Electrical Resistivity Tomography (ERT), Ground Penetrating Radar (GPR) and surface Nuclear Magnetic Resonance (surface NMR) soundings. These non-invasive methods were supported by in-situ sampling of pore water salinity. These will be described in the following.

2.1. Aerial orthophoto

The UAV data was collected using a DJI Phantom 4 (P4) UAV (DJI P4, 2016). The flight was conducted during low tide on July 6, 2022 between 12:41–12:55 LT (local time) with a flight direction of approximately west-east, an altitude of 120 m, and an along-track and cross-track overlap of 85 % and 75 %, respectively. During the flight, meteorological conditions were difficult, with partly cloudy skies and wind speeds of about 8–10 m/s. The flight resulted in 305 RGB images which were processed in Agisoft Metashape Professional software version 1.8.4 to create an orthomosaic for the covered area using image exif information. All images were aligned with accuracy settings set to low and pre-selection based on GPS coordinates. We then computed the sparse point cloud, removed outliers and reconstructed the detailed geometry (bundle adjustment) using a dense point cloud (reconstruction parameters: surface type - height field; quality - medium; depth filter - mild). The resulting digital orthomosaic (DOM) was exported with a ground sampling distance of 3.3 cm and a total error of 4.6 m (x = 4.0 m, y = 1.1). As a final step, the total area covered by the DOM was reduced to the area of interest.

2.2. Electromagnetic induction (EMI)

EMI uses a transmitter coil to produce a harmonic primary electromagnetic field, which induces electrical currents in the subsurface. These currents in turn produce a secondary electromagnetic field, which is measured with a receiver coil. The amplitude difference and phase shift between the primary and secondary magnetic fields depend on the electrical resistivity and magnetic permeability of the subsurface. The penetration depth of the EMI method depends on several factors, including signal frequency, transmitter-receiver distance and orientation, measurement height, and soil properties. For the application of detecting SGD only the electrical resistivity is of interest and thus the in-phase component will be neglected throughout this paper. The EMI method measures the apparent electrical resistivity, which can be used to derive a specific resistivity subsurface model by means of inversion. We conducted measurements using a CMD Explorer (GF Instruments) with horizontal coplanar (HCP) orientation and coil spacings of 1.48 m, 2.82 m, and 4.49 m. The measurements were carried out along profile lines at low tide. We used a sampling interval of 10 Hz (approx. 10 cm inline spacing) and about 5 m profile spacing. The device was carried at 1 m above ground. Accurate positioning was achieved with an RTK-DGPS by Stonex (S9i). For processing we applied following steps: a) a moving average filter over 11 samples applied to the GNSS coordinates; b) correcting the inline and crossline GNSS offsets with respect to the coil-pair midpoints; c) applying a drift correction by comparing crossing points of the areal data with a reference profile (see De Smedt et al., 2016; Costard et al., 2022); d) applying an inline bandpass filter to reduce the noise caused by walking; and e) binning the data onto a rectangular grid of 7 m × 7 m cell size. In the highly conductive tidal flats, the often used Low Induction Number (LIN) approximation (Callegary et al., 2007; Beamish, 2011) is not valid (see e.g. Delefortrie

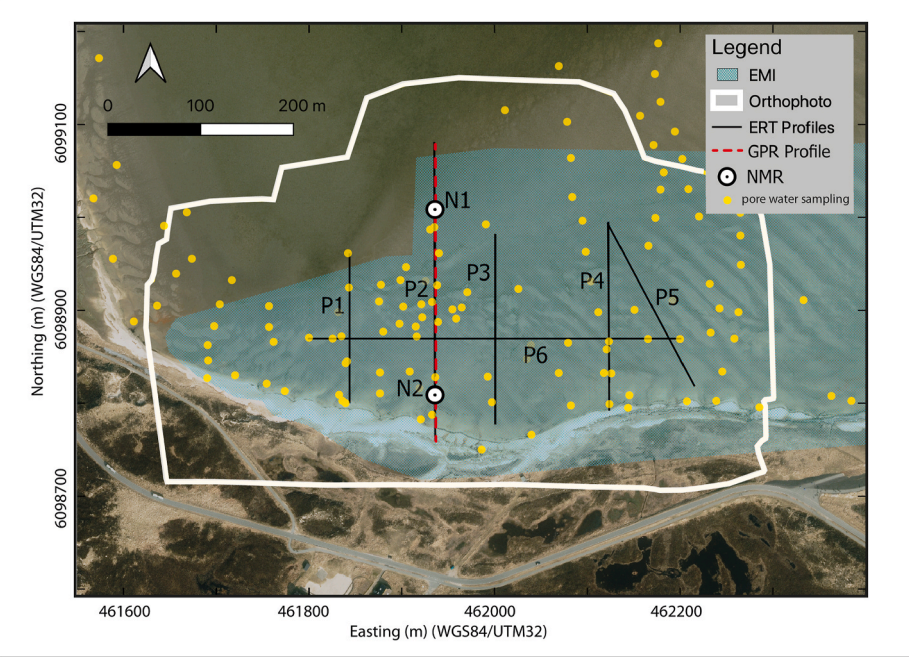

Fig. 2. Location map showing the investigation area as a whole and lines of geophysical profiling in the southern Königshafen bay (Basemap: ©GeoBasis-DE/ LVermGeo SH/CC BY 4.0).

et al., 2014). This has to be taken into account in ECa calculations and subsequent inversion. For each grid cell a 1D inversion was performed using an artificial bee colony algorithm with variable layer number (Wilken et al., 2024) using the exact forward solution of the Maxwell equations (Hanssens et al., 2019). For each inversion 200 iterations were carried out with a population size of 400 models, and with two to four layers in the 50–500 mS/m search space. The best 50 models were averaged and represent the resulting model in the respective grid cell.

2.3. Ground-penetrating radar (GPR)

GPR uses electromagnetic waves in the MHz-GHz frequency range to map shallow subsurface structures and characterize material properties. GPR is a fast and high-resolution method and sensitive to the dielectric permittivity and electrical resistivity, i.e. mainly the water content, salinity and sediment texture (Jol, 2009). The lower the electrical resistivity, the more the electromagnetic waves are attenuated and the lower the depth of investigation. For this reason, seawater and seawater-saturated sediments are generally not considered to be suitable environments for GPR and reflections from the subsurface are not expected to be recorded due to the high wave attenuation on tidal flats. However, GPR can be used effectively in coastal environments to map spots of higher electrical resistivity, i.e. freshwater flow path and FSGD (e.g. de Souza et al., 2021). These high resistivity spots are characterized by windows in the radar section, where reflections from the subsurface can be observed. Another indication of freshwater is the crosstalk amplitude. The crosstalk is the signal that couples directly from the transmitting antenna to the receiving antenna and is influenced by the antenna coupling to the ground. If the subsurface resistivity is high, the energy of the excitation pulse tends to be transmitted into the ground, whereas the energy tends to remain on the antenna causing a stronger crosstalk if the resistivity is low. Therefore, the spots of freshwater SGDs are characterized by lower crosstalk amplitudes than the low resistive saltwater saturated tidal flat sediment. We used a GSSI SIR 4000 GPR with a shielded 200 MHz antenna with a fixed transmitter-receiver distance of 0.3 m that was towed by hand on the tidal flat recording data in a constant offset (CO) configuration. GPR traces were recorded every 5 cm and the position was tracked by a RTK-DGPS. Data processing comprised time-zero correction, dewow filtering and amplitude balancing by compensating for spherical divergence and exponential losses.

2.4. Electrical Resistivity Tomography (ERT)

ERT can be used to determine the distribution of the specific electrical resistivity in soils and sediments, by injecting a current through two electrodes and measuring the potential difference between two additional electrodes. Multi-electrode set-ups along profiles allow for two-dimensional resistivity distributions, where the investigation depth is controlled by the electrode spacing. The apparent electrical resistivity is calculated using Ohm's law and an additional layout dependent geometric factor. However, a depth dependent resistivity model can be reconstructed by data inversion. This describes the process of the model estimation with a forward response that fit the observed data (Everett, 2013). The data has subsequently been inverted using the open-source software PyGimli (Rücker et al., 2017). The measurements were carried out along profile lines at low tide perpendicular and parallel to the shoreline to image subsurface freshwater flow paths also in greater depth (up to 40 m). On the one hand, the ABEM Terrameter LS was used with an equidistant electrode spacing of 2 m and 48 electrodes. The multi gradient array (Dahlin and Zhou, 2006) ensured a quick measuring progress. On the other hand, the towed system uses the Geoserve RESECS together with 24 logarithmically spaced metal spheres as electrodes mounted on a cable. The electrode spacing varies between 0.5 m and 56 m. A total of 6 sections with a length between 100 m and 400 m were measured by towing the ERT system over the tidal flats (see Fig. 2).

2.5. Surface nuclear magnetic resonance (NMR)

The NMR technique can measure the signal emitted from hydrogen protons in the subsurface, providing estimates of subsurface water content and hydraulic conductivity. While NMR is commonly used in laboratory and borehole geophysics, it is also utilized in field geophysics under the name of Magnetic-Resonance-Sounding (MRS). MRS (or surface NMR) employs a large surface loop, typically ranging from 10 to 100 m in diameter, to apply electromagnetic excitation pulses that disturb the hydrogen proton equilibrium state. Once the pulse is turned off, the hydrogen protons relax back to their initial state, emitting a radio signal that can be detected by the surface loop. Most commonly, measurement sequences are used that detect a signal known as the free induction decay (FID). The FID signal amplitude is proportional to the number of hydrogen protons and therefore sensitive to the water content of the subsurface. The relaxation time of the FID provides information about the pore environment, i.e. long relaxation times indicate large pores while short times indicate small pores with water bound at the pore surfaces. Consequently, relaxation times can serve as a proxy for estimates of the hydraulic conductivity. Compared to laboratory NMR, surface NMR has the drawback that very short relaxation times as present in clayey material are too fast to be detected, thus silty/clayey layers appear similar as layers with low water content. By measuring the amplitude and relaxation time of the FID using pulses with a varying pulse moment (product of pulse current and duration), it is possible to obtain a depth distribution of the subsurface properties in a non-invasive manner. For a more detailed insight in the methodology see, for example Hertrich (2008) or Müller-Petke and Yaramanci (2015). Especially in coastal environments a joint application of surface NMR together with electrical resistivity methods enables to distinguish salt water saturated sediments from fine-grained or silty/clayey sediments that often show similar electrical resistivities (Günther and Müller-Petke, 2012).

The measurement was carried out using the GMR system (Vista-Clara). A figure-eight square-loop (Trushkin et al., 1994) layout with 40 m side length and 2 turns was used and oriented north-south to suppress artificial noise sources. To further improve the noise cancellation by applying the remote reference technique (Müller-Petke and Costabel, 2014), an additional remote-reference also as a figure-eight was set-up in 250 m east from the detection loops. We conducted a simple free-induction decay measurement with 40 ms pulse duration leading to a maximum pulse moment of about 10 As. Data processing and inversion was carried out using the open-source MRSmatlab software (Müller-Petke et al., 2016).

2.6. Pore water sampling

Pore water samples were taken during low tide across the study area using stainless steel push point piezometers (1/4″ dia.; MHE Products) and to different depths on several campaigns between March 2021 and July 2022. Pore waters were taken using plastic syringes, and an aliquot equivalent to 3 times the inner sampler volume of the lance was discarded before taking the sample. One aliquot was taken for different geochemical analyses (data not shown). One aliquot was placed in plastic centrifuge vials for future chloride measurement. Depending on the group doing the sampling and analysis, either the chloride concentration (measured on a Metrohm ion chromatograph), electrical conductivity (using a Schott Handylab LF11 or a Hach conductivity meter) or an optical refractometer were used to quantify the salt content of the samples. All results were converted to practical salinity units (PSU) to allow comparison between methods. The results are a combination of values from different depths varying between 80 and 150 cm. Only samples from depths higher than 80 cm were used to avoid the zone of active saltwater recirculation driven by tides.

3. Results

Using UAVs, high-resolution orthophotos were generated to document the tidal flat surface. Electrical resistivity mapping was then conducted across a large area, reaching depths of approximately 5 m, using Electromagnetic Induction (EMI). The geoelectric depth structure was further examined through Electrical Resistivity Tomography (ERT) along selected profiles. Potential FSGD locations on the tidal flat surface were identified with high lateral resolution using Ground Penetrating Radar (GPR), while subsurface water content was assessed through Surface Nuclear Magnetic Resonance (NMR). Finally, in-situ measurements of pore water salinity at the most probable FSGD sites were performed for verification. The results of these methods are presented below.

3.1. Aerial orthophoto and electromagnetic induction (EMI)

The orthophoto of the measurement area (Fig. 3d–g) highlights distinct tidal flat features, which are characterized by brighter surrounding sediments and are often associated with seagrass/algae on the northern side (Fig. 3e and f show a zoomed cutout of the orthophoto within the blue rectangle). The locations marked with pink polygons in Fig. 3g and f displays specific features suggesting a seepage area, coinciding with areas where low salinity was measured. These indicate discharge of fresher groundwater and are, therefore, a first indication for FSGD (Fig. 3a). Most interestingly, these sites are stable over time, as seen in aerial photographs from the last 30 years which show them in the same locations.

The depth-slices of electrical resistivity derived from the EMI inversion (Fig. 3a, b, c) show generally higher values along the

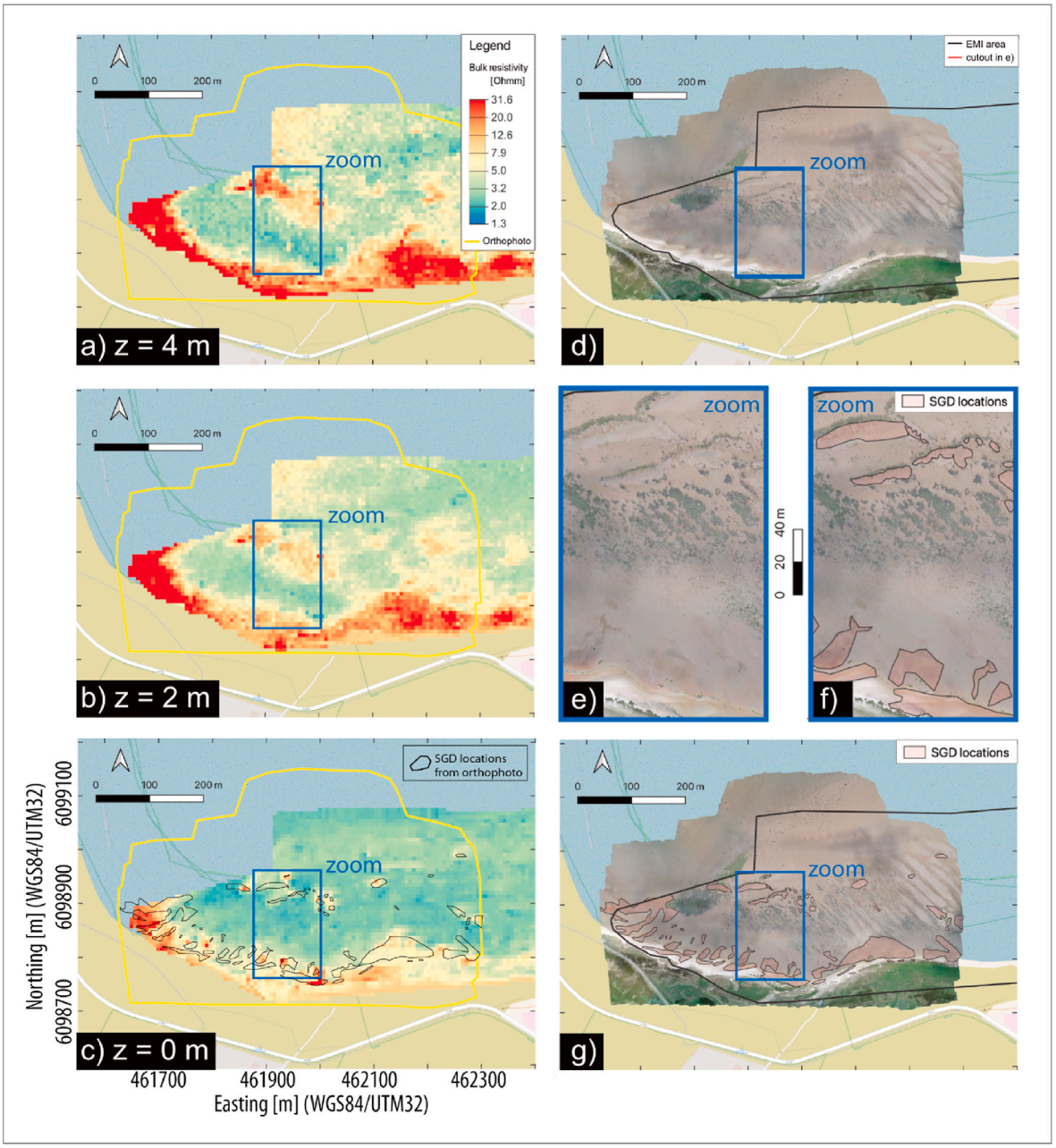

Fig. 3. Maps of bulk sediment resistivity at depths of (a) 4 m, (b) 2 m and (c) at the earth surface derived from the inversion of EMI data. (d) to (g) are orthophotos of the measurement area during low tide (d & g), (e) and (f) show a cutout of the orthophoto with visually detected potential FSGD spots (pink polygons in f and g). Basemap: OpenStreetMap. (For interpretation of the references to color in this figure legend, the reader is referred to the Web version of this article.)

shoreline, especially at greater depths. On the surface (z = 0 m) some small spots of higher resistivity can be seen in the middle of the area that are connected to larger patches in larger depths (Fig. 3c–g). Combining the EMI results with the orthophoto reveals that the distinct areas from the orthophoto correspond to areas with higher resistivity in the EMI depth slices (Fig. 3e–g), suggesting possible FSGD locations.

3.2. Electrical Resistivity Tomography (ERT)

To investigate the discovered potential SGD sites ERT profiles were measured at low tide (Fig. 2). Fig. 4 shows the inversion results of 6 measured geoelectric sections. In general, low resistivities of about 1–5 Ωm are observed in all inversion models (P1 to P6) in the near-surface region down to 2 m depth. However, there are certain locations where the low resistivity layer is interrupted by higher electrical resistivities. Below this layer, resistivities increase to an average of 100 Ωm extending approx. 200 m north of the shoreline, which may indicate freshwater saturated sand layers. Further north in the bay, resistivities of less than 10 Ωm are observed, indicating sands saturated with brackish water and/or clay-containing layers.

In ERT profile P2, the 2–4 m thick low resistive surface layer is interrupted by higher resistivities at locations marked as a, b, c, d in Fig. 4 and c in Fig. 5, indicating freshwater. This layer was identified in borehole D34 (Figs. 1a and 8f), as sand up to 2 m depth (Austen, 1990) and is also present in the ERT section P2. Underneath a high-resistivity layer is observed (>100 Ωm, red colors in Fig. 4), which extends to larger depth.

About 10 m north of D34 a vertical structure of particularly low resistivity is evident in P2 between c and d and at the northern end of P1. This could be caused by either locally increased saltwater or clay content of the sediment.

3.3. Ground-penetrating radar (GPR)

Along the ERT profile P2 (Fig. 2), we recorded GPR data for comparison (Fig. 5a). As expected, GPR shows a generally poor performance with almost no wave penetration due to the high subsurface attenuation that can be expected in saltwater environment. Along most parts of the profile, a horizontal stripe pattern is apparent that is not caused by subsurface structures, but by antenna ringing caused by a mismatch of the antenna impedance due to the low subsurface resistivity. However, there are some small subsections such as at x = 172.5–174.5 m, where GPR performance is moderate and reflections from the subsurface can be observed (inset in Fig. 5a). The antenna crosstalk, i.e. the signal within the first 20 ns, shows some anomalies with weaker amplitudes. These anomalies are well resolved in Fig. 5b which shows the calculated crosstalk energy along the profile. Low values can be observed at x = 30–40 m, 150 m, 170–190 m and in the very southern part of the profile at the shoreline. Most of these anomalies coincide with the parts of the profile where subsurface reflections can be observed. These locations are also characterized by higher subsurface resistivity in the ERT result (marked with a, b, c, d in Fig. 5c).

3.4. Surface nuclear magnetic resonance (NMR)

To identify whether the low resistivity area in ERT profile P2 (Fig. 5c) is due to salt-water or clay, surface NMR measurements were conducted at two positions along the profile (N1 & N2 in Fig. 2). Point N2 close to the shore (x = 50 m) shows almost constant porosities and long relaxation times (between 200 ms and 400 ms) and therefore indicates a sandy deposit (Fig. 5d). The low resistive zone close to the surface (upper 5 m in Fig. 5c) can thus be associated with saltwater infiltration from the tidal dynamics, e.g. showing the upper saline plume.

In contrast, the second NMR sounding N1 (x = 250 m) shows significant dynamics and depth ranges with particular short relaxation times. Even though uncertainties given by gray lines in Fig. 5d are high, the shorter relaxation times indicate fine grained or clayey sediments. Consequently, the low resistivity zone at depth >10 m in this part of the profile is likely not associated with salt water but is interpreted as an aquitard-like structure.

3.5. Pore water sampling

A total of 126 in-situ measurements of pore water salinity were carried out in the depth range from 80 cm to 150 cm. These measurements show that fresh water could be detected in 3 locations, brackish water in 16 locations and salt water in 103 locations. For ground truthing of the potential FSGD spots, indicated by higher resistivity in the EMI and ERT data, we compare the EMI depth slice at 80 cm–150 cm depth with salinities derived from pore water sampling from 80 to 150 cm depth (Fig. 6c). The salinities derived from the pore water samples are represented by dots, with red shades indicating low salinities in the higher resistivity zone along the shoreline and in the vicinity of the

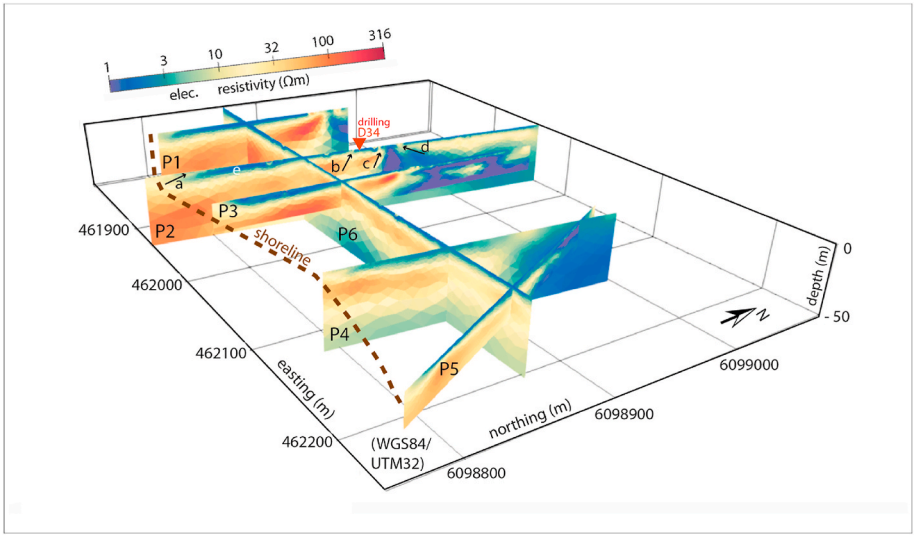

Fig. 4. Electric resistivity-depth sections determined along ERT-profiles P1 to P6 measured during low tide. The letters a,b,c,d indicate locations where structures of higher electrical resistivity come up from the subsurface to the seafloor surface.

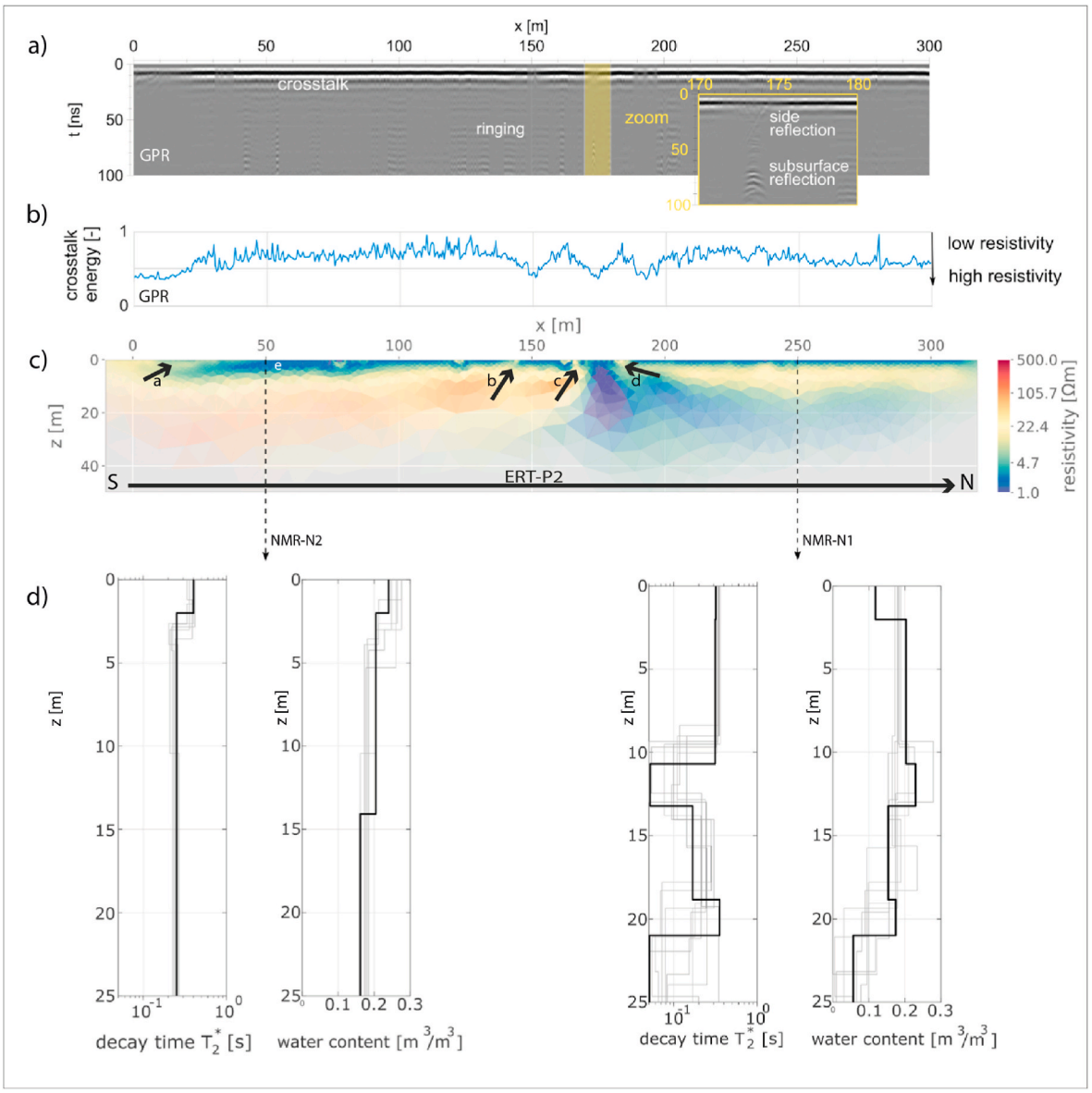

Fig. 5. Comparison of ERT, GPR and NMR along profile P2 (location see Fig. 2): GPR radargram (a), normalized GPR crosstalk energy (b), ERT resistivity-depth section (c), surface NMR soundings at location N1 and N2 (d).

higher resistivity zones in the Königshafen bay. There are a few areas where the measured salinity values do not align with the expectations derived from the EMI maps. This discrepancy may have been caused by different conditions in data collection such as varying tidal cycles at different dates of sampling, sampling depths. The discrepancy can also have been caused by local variation of the clay content of the sediment, to which the electrical resistivity is also sensitive. Still, the overall trend is obvious (Fig. 6c). Therefore, we consider EMI resistivity measurements as a proxy for salinity enabling to locate and investigate FSGD.

In the next step, we determined an empirical relationship between the electrical bulk resistivity (ρ_B) from the EMI results and the in-situ measured salinity (S) of the pore water through a double-logarithmic linear regression yielding

$$\log_{10}(\rho_B) = -0.399 \times \log_{10}(S) + 1.071$$

With a correlation coefficient of 0.8 (Fig. 6a).

Using this relationship, the electrical bulk resistivity values could be converted into pore water salinity. Fig. 6d shows the calculated salinity values for the depth interval of 80 cm–150 cm. This figure must be understood as a first estimate of S applicable only to the sediment conditions at the test site of our study. This is because setting up a more general relation would additionally require also a closer analysis and incorporation of the grain size distribution and porosity (Wunderlich et al., 2013), which is beyond the scope of this paper.

The depth dependence of electrical resistivity and salinity was analyzed at four sites where porewater samples were taken from different depths. The locations P1 and P2 in the vicinity of lowest electrical resistivity at the surface. Locations P3 and P4 are at the potential FSGD zone with higher electrical resistivity near the shoreline (Fig. 6c). The pore water was sampled up to a depth of 1 m, but the EMI inversion results extend to a depth of 5 m. Fig. 7 shows the comparison between resistivity and salinity at these four sites. The x-axes were manually scaled so that both curves cover approximately the same range. In northern part of the bay (Fig. 1a: P1 & P2), at locations P1 and P2 (Fig. 7a and b), lower resistivities of 2.5 Ωm to 4 Ωm and salinities over 20 PSU can be observed, indicating the presence of seawater (Atkinson et al., 1986). In contrast, at locations P3 and P4 (Fig. 7c and d), which are in the vicinity of the coastline, it is observed that the resistivities increase sharply from the surface to depth from approx. 5 Ωm

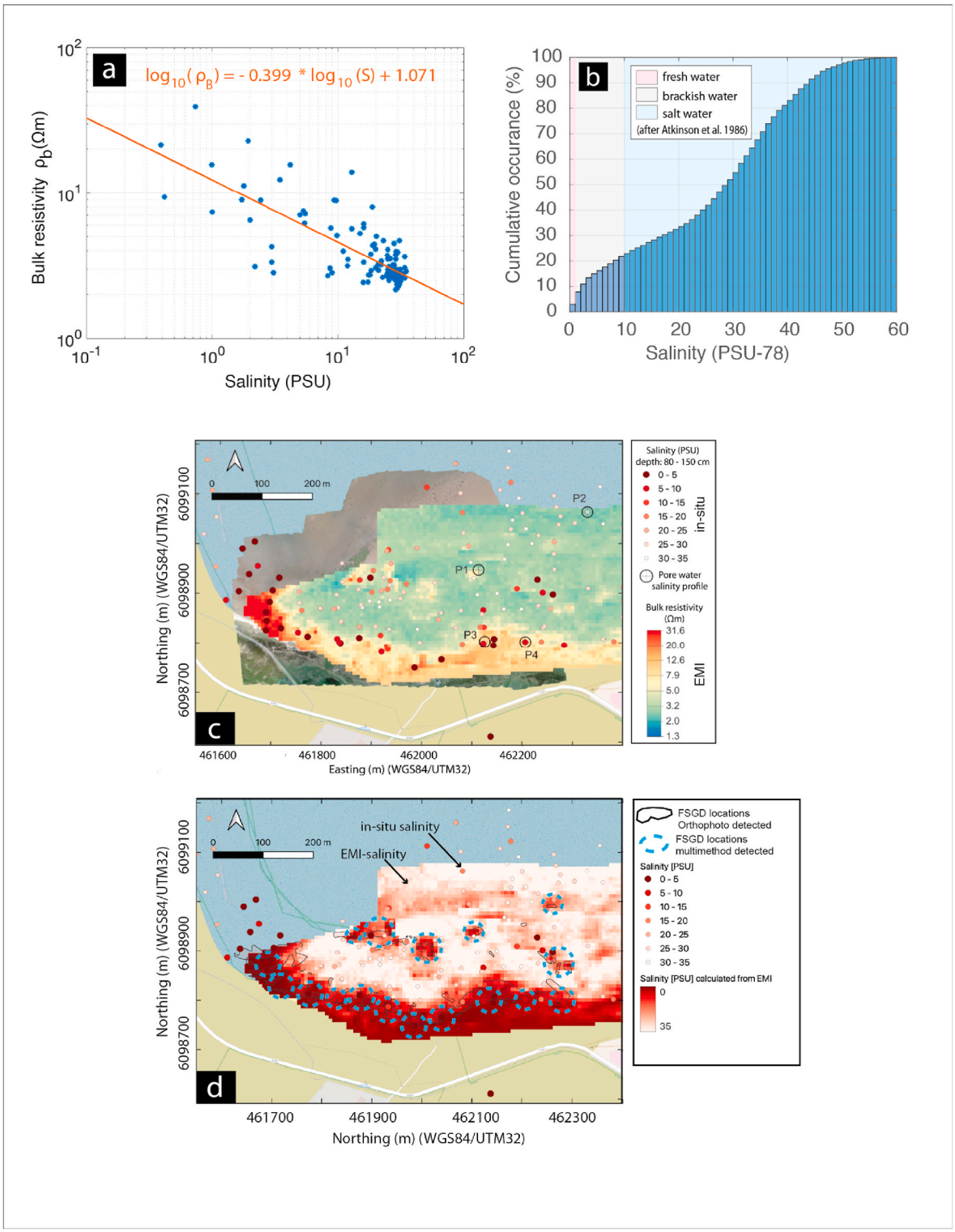

Fig. 6. (a) Cross-plot of bulk electric bulk resistivity inverted from EMI data and salinity of pore water sampled in boreholes at depths between 80 and 150 cm. b) histogram of estimated pore water salinities between depths of 80 cm and 150 cm based on the empirical relationship in figure (a). (c) Depth slice (z: 80 cm–150 cm) of electrical bulk resistivity inverted from EMI data and measured pore water salinity (colored dots). d) Map of estimated pore water salinity at 80 cm–150 cm depth based on the determined empirical relationship in figure (a).

to 20 Ωm, and the salinities decrease sharply from approx. 30 PSU to 2 PSU. According to the resistivities, fresh water can be expected at P3 from about 1.5 m depth and at P4 from about 2.5 m depth. At P3 and P4 we observe a correlation between the resistivity and the salinity in the first meter of depth, but with a shift of about 0.7 m in depth. This can be explained by the smoothing effect of the EMI binning and its lower resolution in the upper first depth meter and can be calibrated based on the salinity results.

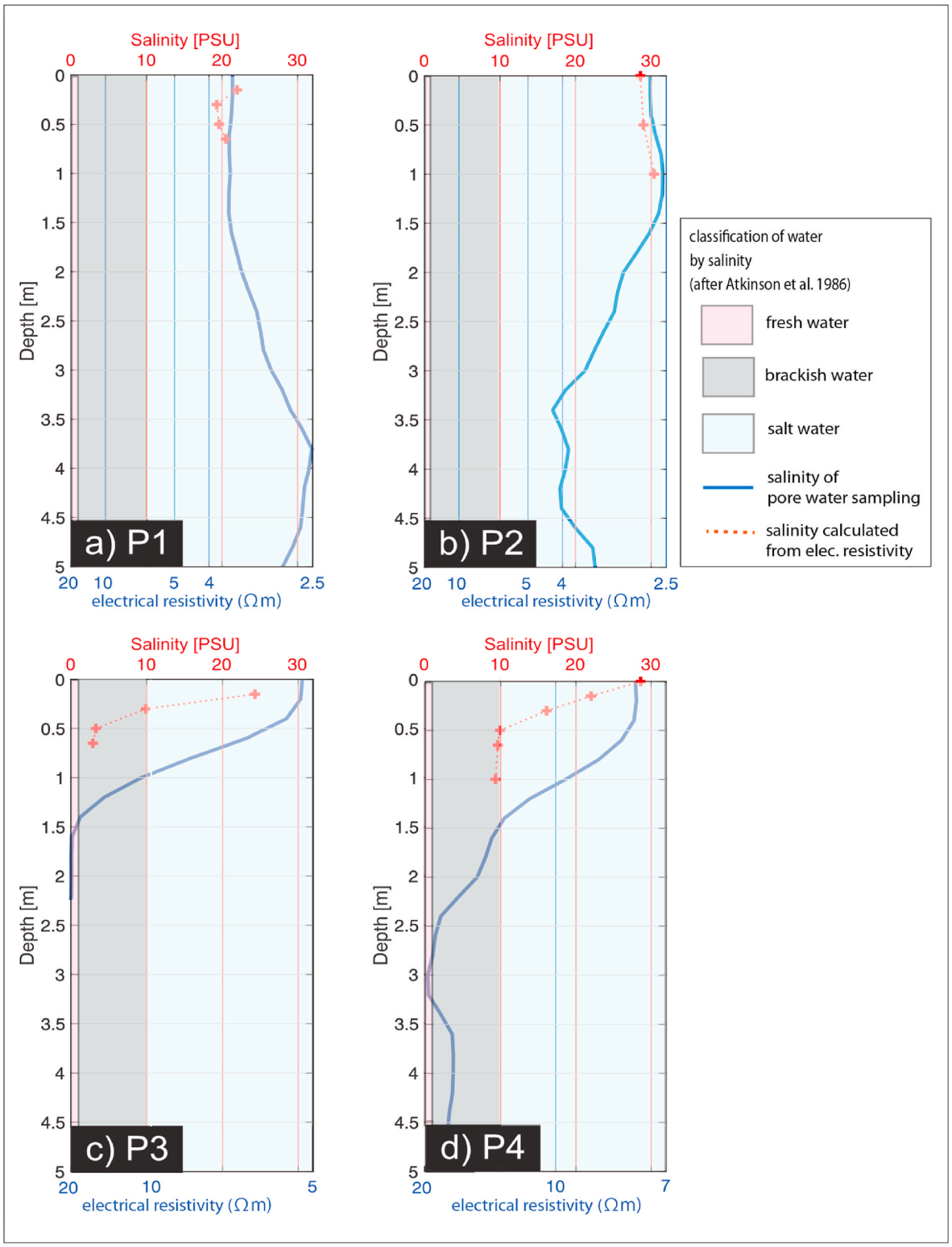

Fig. 7. Comparison between salinities from pore water profiles and bulk electrical resistivities gained from EMI inversion at 4 locations: (a) P1, (b) P2, (c) P3, (d) P4 (Figs. 1a and 6c). Please note the different scaling of the logarithmic resistivity axis. The classification of water based on the salinity (Atkinson et al., 1986) is as follows: fresh water (pink), brackish water (gray), salt water (blue). (For interpretation of the references to color in this figure legend, the reader is referred to the Web version of this article.)

4. Geological and hydrological interpretation

Morphological and very near-surface sedimentary features of the mud flat can be recognized similarly well in the aerial orthophotos and the geophysical maps and sections of ERT, EMI and GPR (Fig. 8).

In the southern part, close to the high tide line, the partial saturation of the sediments on the one hand and the freshwater content in the subsurface on the other hand, lead to higher electrical resistivities (Fig. 8a). Towards the middle of the bay, near-surface tidal flat sediments saturated with seawater lead to significantly lower resistivities

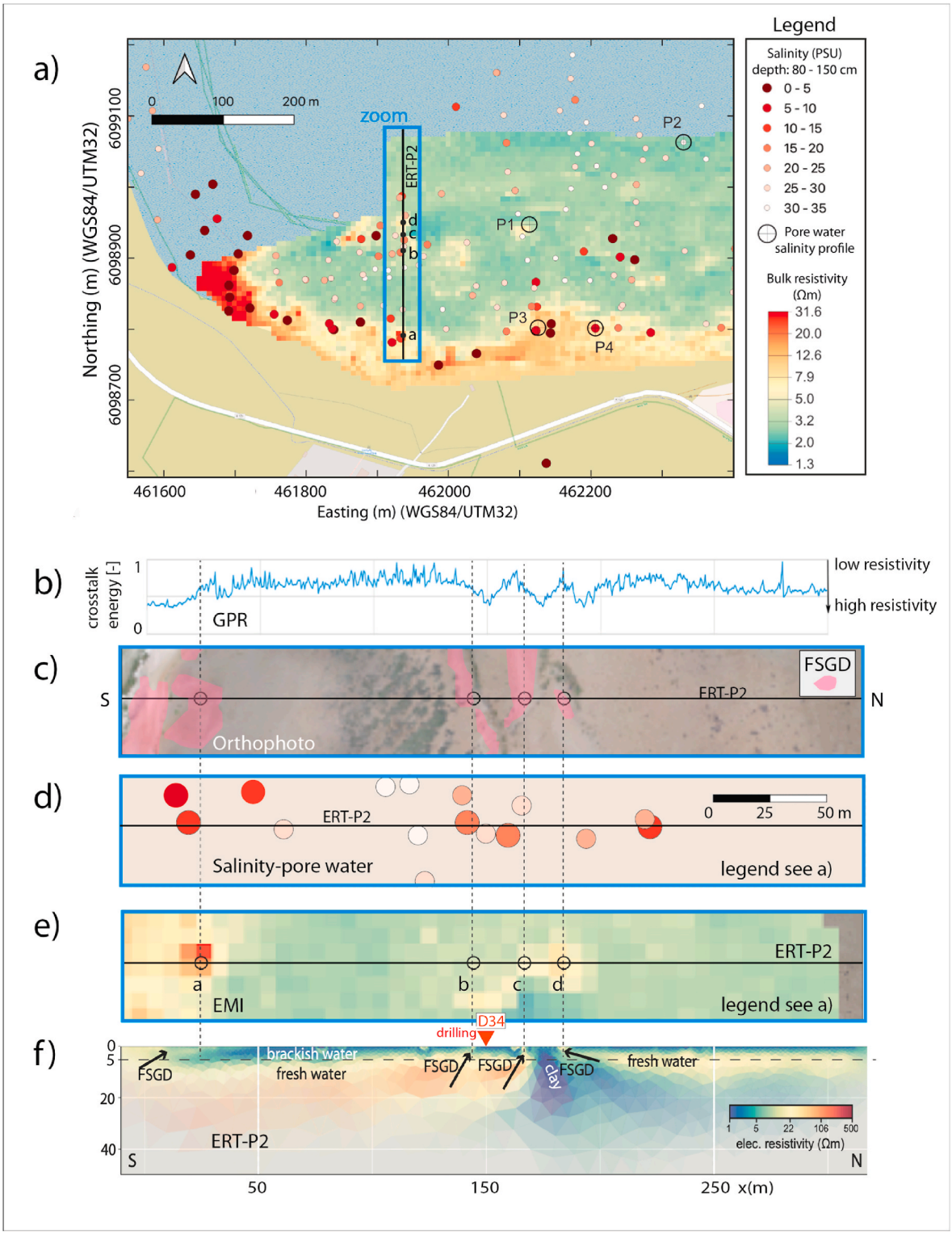

Fig. 8. Combination of geophysical results from EMI, ERT and GPR with pore water salinitiy from downhole sampling and drone aerial orthophotos in the Königshafen bay: (a) map of electric resistivity at 1 m depth from EMI with pore water salinity from sampling (colored spots). (b) GPR crosstalk energy sampled along profile ERT/GPR-P2 (see figure a). (c)–(e) show measurements in the area around profile P2 (blue rectangle in figure a); (c) Cutout of orthophoto with SGD features in pink color; (d) pore water salinity from sampling at 80–150 cm depth; (e) map of electric resistivity; (f) inversion model of ERT-profile P2. (For interpretation of the references to color in this figure legend, the reader is referred to the Web version of this article.)

(<3 Ωm) (Fig. 8a). With the exception of two locations at the ERT-P2 section (x = 90 m & 135 m), the obvious interruptions of higher resistivity in the first layer are consistent with the EMI and GPR results (weak crosstalk amplitude) (Fig. 8b–e,f). These are most likely freshwater seeps. The areal EMI results (Fig. 3) also show that some of the individual freshwater outlets form extensive coherent structures.

For the deeper area (>5 m depth), the ERT shows significantly higher resistivities (Figs. 4 and 8f) (>100 Ωm) over the first 160 m of the

profile, indicating freshwater-saturated sediments (Fig. 8f). The vertical low resistivity anomaly at x ≈ 180 m (between c and d), which extends from the surface to a depth of approx. 20 m and continues to the north, is striking. The southern boundary of this anomaly in the ERT coincides with the lateral reflection in the GPR, which extends towards 174 m and is presumably caused by a sharply defined steep structure (Fig. 5a). A probable explanation is that this is a clay layer spreading out in this area, which may have been deformed by glacial tectonics. In the central part of Königshafen, clay is commonly found in the coring's (Austen, 1990) (Fig. 1) and (Bayerl and Higelke, 1994). This layer represents a groundwater aquitard and is probably the cause of the freshwater seepage on both sides of the structure marked with c and d in Fig. 8f.

5. Discussion

In this study, we employed a combination of measurement techniques to investigate fresh submarine groundwater discharge (FSGD) patterns at different spatial scales, from m to km, at the example location of the Königshafen Bay. The core of our approach consists of combining mapping methods and targeted sampling: we used UAVs for mapping morphological features and vegetational anomalies and areal electromagnetic (EMI) measurements for mapping the bulk electric resistivity of the near-surface sediment layers. Then, targeted downhole pore water sampling was applied to obtain in-situ vales of porewater salinity and to establish a transfer function between bulk resistivity and salinity,

We have shown that large-scale EMI measurements and aerial orthophotos can provide initial indications of FSGD on a tidal flat. These FSGD patches are characterized by a higher electrical resistivity compared to the surrounding area in the EMI data and by brighter surrounding sediments associated with seagrass on the northern side in orthophotos. To further investigate the proposed FSGD patches in the vertical direction, EMI inversions can provide a detailed picture of the shallow subsurface down to 5 m depth, while targeted ERT profiles provide a deeper, detailed, and more focused insights along the profiles. The addition of further surface NMR measurements provides explanations for the occurrence of FSGD spots at exactly these locations, e.g. by distinguishing between clay and saltwater structures that were visible in the ERT profiles as areas of lower resistivity.

Targeted in-situ pore water salinity measurements provide ground truth information for FSGD points identified in the geophysical data, but the number of locations at which this can be carried out is limited. The results of the geophysical methods can therefore be used to extrapolate the point information from the sampling. For this purpose, pore water samples were combined with geophysical measurements, whereby a higher salinity of the pore water was associated with a lower electrical bulk resistivity (Fig. 6a,b,c). The empirical relationship between the electrical bulk resistivity from the EMI results and the in-situ measured salinity of the pore water was calculated (Fig. 6a). Using this relationship, the depth slices of bulk resistivity could be converted into a map of calibrated pore water salinity (Fig. 6d).

Clearly the accuracy of the resulting pore water salinity model (Fig. 6d) is limited by the accuracy of the obtained site-specific resistivity-salinity. The scattering of the data points reflects the heterogeneity of the sediment composition and the limited depth resolution of the geoelectric depth sounding. This could be improved in future studies by using electric direct-push measurements for establishing the empirical relation. Direct-push would also be beneficial for reaching larger depths in pore water sampling. The application of geophysical, hydrogeological and remote sensing methods in SGD research has been demonstrated to be effective over a considerable period of time (Müller, 2010, Müller et al., 2011, Hermans and Paepen, 2020, Hoffmann et al., 2025, Siemon, 2006; Steuer et al., 2007, Igel et al., 2013, Behroozmand et al., 2015, Müller-Petke and Yaramanci, 2015, Tamborski et al., 2015, Lee et al., 2016; Mallast and Siebert, 2019; Oberle et al., 2022, Röper et al., 2014). Our study shows the benefits of a multidisciplinary approach in localizing FSGD zones at meter-scale resolution. In the next step, interdisciplinary multi-method monitoring is needed to deepen the understanding of the dynamic processes.

6. Conclusion

Our field study highlights the benefits of applying an interdisciplinary methodology for identifying and characterizing fresh submarine groundwater discharge (FSGD) in dynamic intertidal environments. By integrating UAV-based orthophotos, geophysical techniques (ERT, EMI, GPR, surface NMR), and in-situ salinity measurements of pore water, we were able to detect and characterize FSGD locations with high reliability.

This new approach allowed us to efficiently detect 17 FSGD locations in the Königshafen bay (Fig. 6d). These areas have a diameter of 30–60 m and are characterized by increased electrical resistivities of 5 Ωm to 30 Ωm and decreased salinity of 0–10 PSU with respect to the surrounding areas (Fig. 6c and d). Approximately 20 % of the surveyed area shows FSGD locations (Fig. 6d), which could be investigated down to a depth of 30 m (Fig. 8f).

Without the large-scale electrical resistivity maps from the electromagnetics and the surface morphology from the orthophotos, half of the suspect locations would not have been detected. But the final verification of whether these are actually FSGD sites could only be performed with the help of ERT, NMR and in-situ pore water investigations. GPR signals were very strongly attenuated by the saline tidal flat surface due to its low electrical resistivity. Only in areas where fresh water is found directly at the surface of the tidal flat GPR showed some depth penetration, which may be regarded as an indirect FSGD indication.

The novelty of this approach lies in the combination of methods whose strengths complement each other as follows.

1) UAV orthophotos and large-scale EMI measurements enable rapid and non-invasive pre-mapping of FSGD-specific features.
2) In-situ measured pore water salinities contribute to the detection of fresh pore water on the tidal flat surface and in the shallow subsurface down to a depth of 1.5 m. Through EMI and ERT measurements the salinity estimates could be extended to larger depth of 5–10 m.
3) Targeted ERT and surface NMR measurements provide detailed insights into the deeper subsurface as well as the layer structure, pore water content and electrical resistivity of the pore water, which is directly related to the salinity of the sediments.

Finally, it is very important to verify the suspected FSGD locations derived from the large-scale mapping with in-situ pore water samples and calibrate them so that pore water salinity maps can be generated for different depths. Our methodology can be regarded as an approach to up-scaling local findings from boreholes to larger areas through electromagnetic measurements.

CRediT authorship contribution statement

Ercan Erkul: Writing – original draft, Visualization, Validation, Methodology, Investigation, Conceptualization. **Tina Wunderlich:** Writing – original draft, Visualization, Software, Methodology, Investigation. **Dennis Wilken:** Visualization, Software, Methodology, Investigation. **Jan Igel:** Visualization, Software, Methodology, Investigation. **Mike Müller-Petke:** Visualization, Validation, Software, Methodology, Investigation. **Mathias Ronczka:** Visualization, Software, Investigation, Data curation. **Tobias Splith:** Visualization, Software, Investigation. **Simon Fischer:** Visualization, Software, Investigation, Data curation. **Benjamin Gilfedder:** Visualization, Software, Investigation. **Michael Ernst Böttcher:** Writing – original draft, Validation, Methodology, Investigation, Conceptualization. **Cátia M. Ehlert von Ahn:** Visualization, Investigation. **Ralf Gründling:** Visualization, Investigation. **Jasper Hoffmann:** Visualization, Investigation. **Anna-Kathrina Jenner:** Visualization, Investigation. **Erman Lu:** Visualization,

Investigation. **Till Oehler:** Visualization, Investigation. **Wolfgang Rabbel:** Writing – original draft, Methodology, Investigation, Conceptualization. **Lasse Sander:** Writing – original draft, Visualization, Investigation. **Jan Scholten:** Writing – original draft, Investigation. **Franz Schulze:** Visualization, Investigation. **Nils Moosdorf:** Writing – original draft, Methodology, Investigation, Conceptualization. **Ulf Mallast:** Writing – original draft, Visualization, Methodology, Conceptualization.

Declaration of competing interest

The authors declare that they have no known competing financial interests or personal relationships that could have appeared to influence the work reported in this paper.

Acknowledgements

We would like to thank the German Research Foundation (DFG) for supporting the KiSNet-Projekt (MA7041/6–1). The investigations further contribute to the BMBF project COOLSTYLE/CARBOSTORE. MEB further wishes to thank Patricia Roeser, and Antonia Schell for their support in the field.

We would like to thank the Landesbetrieb für Küstenschutz, Nationalpark und Meeresschutz Schleswig-Holstein (Kai Eskildsen, Moritz Padlat) for their support to work in the protected areas, and before and during the field campaigns.

We would like to thank all Master and Bachelor students of the University of Bayreuth participating in the Geoecology program and all students from the University Oldenburg who supported the field surveys.

We would like to thank the Diedrichsen family for the support carrying out field measurements.

We would like to thank Dieter Epping and Johanna Volk for supporting the field surveys.

We would like to thank Gitta von Rönn for the graphical visualization of the drilling results.

We would like to thank AXIO-NET for the supply of precise real-time GNSS correction data.

Data availability

The data that has been used is confidential.

References

Annan, A.P., 2009. Electromagnetic principles of ground penetrating radar. In: Jol, H.M. (Ed.), Ground Penetrating Radar: Theory and Applications. Elsevier, Amsterdam, the Netherlands, pp. 3–40.

Atkinson, S.F., Miller, G.D., Curry, D.S., Lee, S.B., 1986. Salt Water Intrusion Status and Potential in the Contiguous United States. CRC Press. ISBN 13:978-1-315-89743-1 (hbk), ISBN 13: 978-1-351-07653-1 (ebk).

Austen, I., 1990. Geologisch-sedimentologische Kartierung des Königshafens (List auf Sylt) und Untersuchung seiner Sedimente. Dipl.Arb. Univ., Kiel, p. 99.

Austen, I., 1992. Geologisch-sedimentologische Kartierung des Königshafens (List/Sylt). Meyniana 44, 45–52.

Bayerl, K.A., Higelke, B., 1994. The development of northern sylt during the latest Holocene. Helgol. Meeresunters. 48, 145–162. https://doi.org/10.1007/bf02367032.

Beamish, D., 2011. Low induction number, ground conductivity meters: a correction procedure in the absence of magnetic effects. J. Appl. Geophys. 75 (2), 244–253. https://doi.org/10.1016/j.jappgeo.2011.07.005, 2011, ISSN 0926-9851.

Behroozmand, A.A., Keating, K., Auken, E., 2015. A review of the principles and applications of the NMR technique for near-surface characterization. Surv. Geophys. 36, 27–85.

Böttcher, M.E., Mallast, U., Massmann, G., Moosdorf, N., Müller-Petke, M., Waska, H., 2024. Coastal-groundwater interfaces (submarine groundwater discharge). In: Krause, S., Hannah, D.M., Grimm, D.B. (Eds.), Ecohydrological Interfaces. Wiley Science, pp. 123–148.

Burnett, W.C., Aggarwal, P.K., Aureli, A., Bokuniewicz, H., Cable, J.E., Charette, M.A., Kontar, E., Krupa, S., Kulkarni, K.M., Loveless, A., Moore, W.S., Oberdorfer, J.A., Oliveira, J., Ozyurt, N., Povinec, P., Privitera, A.M.G., Rajar, R., Ramessur, R.T., Scholten, J., Stieglitz, T., Taniguchi, M., Turner, J.V., 2006. Quantifying submarine groundwater discharge in the coastal zone via multiple methods. Sci. Total Environ. 367, 498–543.

Callegary, J., Ferré, T., Groom, R., 2007. Vertical spatial sensitivity and exploration depth of low-induction-number electromagnetic-induction instruments. Vadose Zone J. 6, 158–167. https://doi.org/10.2136/vzj2006.0120.

Chand, S., Bollard, B., 2021. Detecting the spatial variability of seagrass meadows and their consequences on associated macrofauna benthic activity using novel drone technology. Remote Sens. 14 (1), 160.

Costard, L., Wunderlich, T., Grüneberg-Wehner, K., Wolf, F.N., Erkul, E., Gräber, M., Rabbel, W., 2022. The deserted manor of noer, Schleswig-Holstein, Germany. Geophysical prospection methods in comparison. J. Environ. Eng. Geophys. 27 (1), 33–44. https://doi.org/10.32389/JEEG21-023.

Curcio, A.C., Barbero, L., Peralta, G., 2023. UAV-Hyperspectral imaging to estimate species distribution in salt marshes: a case study in the Cadiz Bay (SW Spain). Remote Sens. 15 (5), 1419.

Cyronak, T., Santos, I.R., Erler, D.V., Eyre, B.D., 2013. Groundwater and porewater as major sources of alkalinity to a fringing coral reef lagoon (Muri Lagoon, Cook Islands). Biogeosciences 10, 2467–2480. https://doi.org/10.5194/bg-10-2467-2013.

D'Elia, C.F., Webb, K.L., Porter, J.W., 1981. Nitrate-rich groundwater inputs to discovery Bay, Jamaica: a significant source of N to local coral reefs. Bull. Mar. Sci. 1981, 903–910, 31. Jg., Nr. 4.

Dahlin, T., Zhou, B., 2006. Multiple-gradient array measurements for multichannel 2D resistivity imaging. Near Surf. Geophys. 4 (2), 113–123. https://doi.org/10.3997/1873-0604.2005037.

De Smedt, P., Delefortrie, S., Wyffels, F., 2016. Identifying and removing micro-drift in ground-based electromagnetic induction data. Appl. Geophys. 131, 14–22.

De Souza, G.K., da Guia Albuquerque, M., da Silva, C.A.B., Nienchesk, L.F.H., de Andrade, C.F.F., 2021. Washouts as a source of dissolved elements to the coastal ocean in southern Brazil and its hydrogeological characteristics. Regional Studies in Marine Science 41, 101547. https://doi.org/10.1016/j.rsma.2020.101547.-007-0090-7.

Delefortrie, S., De Smedt, P., Saey, T., Van De Vijver, E., Meirvenne, M., 2014. An efficient calibration procedure for correction of drift in EMI survey data. J. Appl. Geophys. 110. https://doi.org/10.1016/j.jappgeo.2014.09.004.

DJI P4 user manual v1.0. Available online: https://dl.djicdn.com/downloads/phantom_4_pro/Phantom+4+Pro+Pro+Plus+User+Manual+v1.0.pdf–. (Accessed 22 July 2024).

Dolch, T., Hass, H.C., 2008. Long-term changes of intertidal and subtidal sediment compositions in a tidal basin in the northern Wadden Sea (SE north Sea). Helgol. Mar. Res. 62, 3–11. https://doi.org/10.1007/s10152.

Everett, Mark E., 2013. Near-Surface Applied Geophysics. Cambridge University Press, 2013. ProQuest Ebook Central. http://ebookcentral.proquest.com/lib/christianalbrechts/detail.action?docID=1139683.

Garrison, G.H., Glenn, C.R., McMurtry, G.M., 2003. Measurement of submarine groundwater discharge in Kahana Bay, O'ahu, Hawai'i. Limnol. Oceanogr. 48, 920–928. https://doi.org/10.4319/lo.2003.48.2.0920.

Goldschmidt, P., Bayerl, K., Austen, I., Köster, R., 1993. From the Wanderdfinen to the Watt: coarse-grained aeolian sediment transport on Sylt, Germany. Z. Geomorphol. 37, 171–178.

Gripp, K., Simon, W.G., 1940. Untersuchungen über den Aufbau und die Entstehung der Insel Sylt. I. Nord-Sylt. Westküste 2 (2/3), 24–70.

Günther, T., Müller-Petke, M., 2012. Hydraulic properties at the north sea island of Borkum derived from joint inversion of magnetic resonance and electrical resistivity soundings. Hydrol. Earth Syst. Sci. 16 (9), 3279–3291.

Hanssens, D., Delefortrie, S., De Pue, J., Van Meirvenne, M., De Smedt, P., 2019. Frequency-domain electromagnetic forward and sensitivity modeling: practical aspects of modeling a magnetic dipole in a multilayered half-space. IEEE Geoscience and Remote Sensing Magazine 7 (1), 74–85. https://doi.org/10.1109/MGRS.2018.2881767.

Hermans, T., Paepen, M., 2020. Combined inversion of land and marine electrical resistivity tomography for submarine groundwater discharge and saltwater intrusion characterization. Geophys. Res. Lett. 47 (3).

Hertrich, M., 2008. Imaging of groundwater with nuclear magnetic resonance. Prog. Nucl. Magn. Reson. Spectrosc. 53 (4), 227–248.

Hoffmann, J.J.L., Schneider von Deimling, J., Schröder, J.F., Schmidt, M., Held, P., Crutchley, G.J., et al., 2020. Complex eyed pockmarks and submarine groundwater discharge revealed by acoustic data and sediment cores in Eckernförde Bay, SW Baltic sea. G-cubed 21 (4), e2019GC008825.

Hoffmann, J.J., Mountjoy, J.J., Spain, E., Gall, M., Tait, L.W., Ladroit, Y., Micallef, A., 2023. Fresh submarine groundwater discharge offshore Wellington (new Zealand): hydroacoustic characteristics and its influence on seafloor geomorphology. Front. Mar. Sci. 10, 1204182.

Hoffmann, J.J., Erkul, E., Fischer, S., Yolcubal, I., Yogeshwar, P., Rabbel, W., et al., 2025. Bridging land and sea: geophysical insights into coastal karstic groundwater dynamics, freshwater plumes and saltwater intrusions in the urban regions of Antalya (Türkiye). J. Hydrol.: Reg. Stud. 57, 102145.

Igel, J., Günther, T., Kunzer, M., 2013. Ground-penetrating radar insight into a coastal aquifer: the freshwater lens of Borkum island. Hydrol. Earth Syst. Sci. 17, 519–531. https://doi.org/10.5194/hess-17-519-2013.

Jiang, C., Müller-Petke, M., Lin, J., Yaramanci, U., 2015. Magnetic resonance tomography using elongated transmitter and in-loop receiver arrays for time-efficient 2-D imaging of subsurface aquifer structures. Geophys. J. Int. 200 (2), 824–836.

Johannes, R.E., Hearn, C.J., 1985. The effect of submarine groundwater discharge on nutrient and salinity regimes in a coastal lagoon off Perth, Western-Australia. Estuar. Coast Shelf Sci. 21 (6), 789–800.

Jol, H. (Ed.), 2009. Ground Penetrating Radar: Theory and Applications. Elsevier. https://doi.org/10.1016/b978-0-444-53348-7.x0001-4.
Kim, K.L., Kim, B.J., Lee, Y.K., Ryu, J.H., 2019. Generation of a large-scale surface sediment classification map using unmanned aerial vehicle (UAV) data: a case study at the Hwang-do tidal flat, Korea. Remote Sens. 11 (3), 229.
Kreuzburg, M., Scholten, J., Hsu, F.H., Liebetrau, V., Sültenfuß, J., Rapaglia, J., Schlüter, M., 2023. Submarine groundwater discharge-derived nutrient fluxes in Eckernförde Bay (Western Baltic Sea). Estuaries Coasts 46, 1190–1207. https://doi.org/10.1007/s12237-023-01202-0.
Kwon, E.Y., Kim, G., Primeau, F., Moore, W.S., Cho, H.-M., DeVries, T., Sarmiento, J.L., Charette, M.A., Cho, Y.-K., 2014. Global estimate of submarine groundwater discharge based on an observationally constrained radium isotope model. Geophys. Res. Lett. 41, 8438–8444. https://doi.org/10.1002/2014GL061574.
Lecher, A.L., Mackey, K.R.M., 2018. Synthesizing the effects of submarine groundwater discharge on marine biota. Hydrology 5, 60.
Lee, E., Yoon, H., Hyun, S.P., Burnett, W.C., Koh, D.C., Ha, K., et al., 2016. Unmanned aerial vehicles (UAVs)-based thermal infrared (TIR) mapping, a novel approach to assess groundwater discharge into the coastal zone. Limnol Oceanogr. Methods 14 (11), 725–735.
Lindhorst, S., Betzler, C., Hass, H.C., 2008. The sedimentary architecture of a Holocene barrier spit (Sylt, German Bight): Swash-bar accretion and storm erosion. Sediment. Geol. 206 (1–4), 1–16.
Lindhorst, S., Fuerstenau, J., Christian Hass, H., Betzler, C., 2010. Anatomy and sedimentary model of a hooked spit (Sylt, southern north sea). Sedimentology 57 (4), 935–955.
Lindhorst, S., Betzler, C., Hass, H.C., 2013. Large scale architecture of a stacked Holocene spit – the stratigraphy of northern Sylt (southern North sea). [Großmassstäbliche Architektur eines holozänen Nehrungshakens – die Stratigrafie von Nord-Sylt (südliche Nordsee).]. Z. Dt. Ges. Geowiss. 164, 63–79. Stuttgart.
Luijendijk, E., Gleeson, T., Moosdorf, N., 2020. Fresh groundwater discharge insignificant for the world's oceans but important for coastal ecosystems. Nat. Commun. 11, 1260. https://doi.org/10.1038/s41467-020-15064-8, 2020.
Luoma, S., Majaniemi, J., Pullinen, A., Mursu, J., Virtasalo, J.J., 2021. Geological and groundwater flow model of a submarine groundwater discharge site at Hanko (Finland), northern Baltic sea. Hydrogeol. J. https://doi.org/10.1007/s10040-021-02313-3.
Mallast, U., Siebert, C., 2019. Combining continuous spatial and temporal scales for SGD investigations using UAV-Based thermal infrared measurements. Hydrol. Earth Syst. Sci. 23, 1375–1392. https://doi.org/10.5194/hess-23-1375-2019.
Mallast, U., Gloaguen, R., Friesen, J., Rödiger, T., Geyer, S., Merz, R., Siebert, C., 2014. How to identify groundwater-caused thermal anomalies in lakes based on multi-temporal satellite data in semi-arid regions. Hydrol. Earth Syst. Sci. 18 (7), 2773–2787.
Mejías, M., Ballesteros, B.J., Antón-Pacheco, C., Domínguez, J.A., Garcia-Orellana, J., Garcia-Solsona, E., Masqué, P., 2012. Methodological study of submarine groundwater discharge from a karstic aquifer in the Western Mediterranean Sea. J. Hydrol. 464–465, 27–40. https://doi.org/10.1016/j.jhydrol.2012.06.020.
Moore, W.S., 1999. The subterranean estuary: a reaction zone of ground water and sea water. Mar. Chem. 65, 111–125. https://doi.org/10.1016/S0304-4203(99)00014-6.
Moore, W.S., 2010. The effect of submarine groundwater discharge on the ocean. Ann. Rev. Mar. Sci 2, 59–88. https://doi.org/10.1146/annurev-marine-120308-081019.
Moore, W.S., Sarmiento, J.L., Key, R.M., 2008. Submarine groundwater discharge revealed by 228Ra distribution in the upper Atlantic Ocean. Nat. Geosci. 1, 309–311. http://www.nature.com/ngeo/journal/v1/n5/suppinfo/ngeo183_S1.html.
Moosdorf, N., Stieglitz, T., Waska, H., Dürr, H.H., Hartmann, J., 2015. Submarine groundwater discharge from tropical islands: a review. Grundwasser 20, 53–67. https://doi.org/10.1007/s00767-014-0275-3.
Moosdorf, N., Böttcher, M.E., Adyasari, D., Erkul, E., Gilfedder, B., Greskowiak, J., Jenner, A.-K., Kotwicki, L., Massmann, G., Mueller-Pethke, M., Oehler, T., Post, V., Prien, R., Scholten, J., Siemon, B., von Ahn, C.M.E., Walther, M., Waska, H., Wunderlich, Mallast U., 2021. A state-of-the-art perspective on the characterization of subterranean estuaries at the regional scale. Front. Earth Sci. 9, 601293, 1-26.
Müller, H., 2010. Characterization of Marine near-surface Sediments by Electromagnetic Profiling. Universität Bremen, Bremen. Dissertation.
Müller, H., Dobeneck, T., Hamer, K., 2011. Near-surface electromagnetic, rock magnetic, and geochemical fingerprinting of submarine freshwater seepage at Eckernförde Bay (SW Baltic sea). Geo Mar. Lett. 31, 123–140.
Müller-Petke, M., Yaramanci, U., 2015. 11.13-Tools and techniques: nuclear magnetic resonance. Treatise on geophysics 11, 419–445.
Müller-Petke, M., Braun, M., Hertrich, M., Costabel, S., Walbrecker, J., 2016. MRSmatlab -A software tool for processing, modeling, and inversion of magnetic resonance sounding data. Geophysics 81 (4), WB9–WB21.
Müller-Petke, M., Costabel, S., 2014. Comparison and optimal parameter settings of reference-based harmonic noise cancellation in time and frequency domains for surface-NMR. Near Surf. Geophys. 12 (2), 199–210.
Oberle, F.K., Prouty, N.G., Swarzenski, P.W., Storlazzi, C.D., 2022. High-resolution observations of submarine groundwater discharge reveal the fine spatial and temporal scales of nutrient exposure on a coral reef: Faga'alu, AS. Coral Reefs 41 (4), 849–854.
Oehler, T., Ramasamy, M., Moosdorf, N., Dähnke, K., Ankele, M., Böttcher, M.E., Santos, I.R., Babu, S., 2021. Tropical beaches attenuate groundwater nitrogen pollution flowing to the ocean. Environ. Sci. Technol. 55, 8432–8438.
Povinec, P.P., Burnett, W.C., Beck, A., Bokuniewicz, H., Charette, M., Gonneea, M.E., Groening, M., Ishitobi, T., Kontar, E., Liong Wee Kwong, L., Marie, D.E.P., Moore, W. S., Oberdorfer, J.A., Peterson, R., Ramessur, R., Rapaglia, J., Stieglitz, T., Top, Z., 2012. Isotopic, geophysical and biogeochemical investigation of submarine groundwater discharge: IAEA-UNESCO intercomparison exercise at Mauritius island. J. Environ. Radioact. 104, 24–45. https://doi.org/10.1016/j.jenvrad.2011.09.009.
Reise, K., Herre, E., Sturm, M., 2007. Mudflat biota since the 1930s: change beyond return? Helgol. Mar. Res. 62, 13. https://doi.org/10.1007/s10152-007-0087-2.
Röper, T., Greskowiak, J., Massmann, G., 2014. Detecting small groundwater discharge springs using handheld thermal infrared imagery. Groundwater 52 (6), 936–942.
Rücker, C., Günther, T., Wagner, F.M., 2017. pyGIMLi 2017. An open-source library for modeling and inversion in geophysics. Comput. Geosci. 109, 106–123. https://doi.org/10.1016/j.cageo.2017.07.011, 2017.
Santos, I.R., Eyre, T.D., Huettel, M., 2012. The driving forces of porewater and groundwater flow in permeable coastal sediments: a review. Estuar. Coast Shelf Sci. 98, 1–15. https://doi.org/10.1016/j.ecss.2011.10.024.
Schmidt, E., 1974. Nachrichten von der Insel Sylt - Zusammengetragen 1758 von Martin Richard Flor. Nord. Jahrb. 10, 41.
Siemon, B., 2006. Airborne techniques. In: Kirsch, R. (Ed.), Groundwater Geophysics - a Tool for Hydrogeology. Springer, Berlin Heidel-berg, pp. 348–362.
Steuer, A., Siemon, B., Auken, E., 2007. A comparison of helicopter-borne electromagnetics in frequency- and time-domain at the Cuxhaven valley in northern Germany. J. Appl. Geophys. 67, 194–205.
Szymczycha, B., Böttcher, M.E., Ehlert von Ahn, C.M., Diak, M., Koziorowska-Makuch, K., Kuliński, K., Makuch, P., Winogradow, A., 2023. The benthic-pelagic coupling affects the surface water carbonate system above groundwater-charged coastal sediments. Front. Mar. Sci. 1–14, 10:1218245.
Tamborski, J.J., Rogers, A.D., Bokuniewicz, H.J., Cochran, J.K., Young, C.R., 2015. Identification and quantification of diffuse fresh submarine groundwater discharge via airborne thermal infrared remote sensing. Rem. Sens. Environ. 171, 202–217.
Taniguchi, M., 2002. Tidal effects on submarine groundwater discharge into the ocean. Geophys. Res. Lett. 29, 9–11. https://doi.org/10.1029/2002GL014987.
Trushkin, D., Shushakov, O., Legchenko, A., 1994. The potential of a noise-reducing antenna for surface NMR groundwater surveys in the earth's magnetic field. Geophys. Prospect. 42 (8), 855–862.
Waska, H., Kim, G., 2011. Submarine groundwater discharge (SGD) as a main nutrient source for benthic and water-column primary production in a large intertidal environment of the Yellow sea. J. Sea Res. 65, 103–113.
Wilken, D., Mercker, M., Fischer, P., Vött, A., Erkul, E., Corradini, E., Pickartz, N., 2024. Artificial bee colony algorithm with adaptive parameter space dimension: a promising tool for geophysical electromagnetic induction inversion. Remote Sens. 16, 470. https://doi.org/10.3390/rs16030470, 2024.
Wilson, S.J., Moody, A., McKenzie, T., Luijendijk, E., Bayani, Cardenas M., Sawyer, A., Wilson, A., Michael, H., Xu, B., Knee, K., Cho, H.-M., Weinstein, Y., Paytan, A., Moosdorf, N., Chen-Tung, C., Beck, M., Lopez, C., Murgulet, D., Kim, G., Charette, M., Waska, H., Ibánhez, S.P., Gwénaëlle, C., Oehler, T., Onodera, S.I., Saito, M., Rodellas, V., Dimova, N., Montiel, D., Dulai, H., Du, J., Petermann, E., Chen, C.-X., Davis, K., Sugimoto, R., Wang, G., Li, H., Torres, A., Demir, C., Bristol, E., Connolly, C.T., McClelland, J.W., Januario, B., Lamontagne, S., Kumar, B. S.K., Viswanadham, R., Sarma, V.V.S.S., Silva-Filho, E., Shiller, A., Alana, Lecher, Tamborski, J., Bokuniewicz, H., Rocha, C., Reckhardt, A., Böttcher, M.E., Shan, J., Stieglitz, T., Charbonnier, C., Anschutz, P., Terrones, L.M.H., Babu, S., Szymczycha, B., Chen, X., Jinzhou, D., Sadat-Noori, M., Niencheski, F., Null, K., Song, B., Anderson, I.C., Santos, I.R., 2024. Global subterranean estuaries modify groundwater nutrient loading to the ocean. Limnol Oceanogr. Methods (in press).
Wunderlich, T., Petersen, H., al Hagrey, S.A., Rabbel, W., 2013. Pedophysical models for resistivity and permittivity of partially water-saturated soils. Vadose Zone J. 12, 4. https://doi.org/10.2136/vzj2013.01.0023.
Zipperle, A., Reise, K., 2005. Freshwater springs on intertidal sand flats cause a switch in dominance among polychaete worms. J. Sea Res. 54, 143–150. https://doi.org/10.1016/j.seares.2005.01.003.